PHYSICAL REVIEW D **87,** 094506 (2013)

Structure and flow of the nucleon eigenstates in lattice QCD

M. Selim Mahbub, Waseem Kamleh, Derek B. Leinweber, Peter J. Moran, and Anthony G. Williams

Special Research Centre for the Subatomic Structure of Matter, School of Chemistry and Physics, University of Adelaide, South Australia 5005, Australia

(Received 14 February 2013; published 15 May 2013)

A determination of the excited energy eigenstates of the nucleon, $s = \frac{1}{2}$, $I = \frac{1}{2}$, $N^{\pm}$, is presented in full QCD using $2 + 1$ flavor PACS-CS gauge configurations. The correlation-matrix method is used and is built using standard nucleon interpolators employing smearings at the fermion sources and sinks. We develop and demonstrate a new technique that allows the eigenvectors obtained to be utilized to track the propagation of the intrinsic nature of energy states from one quark mass to the next. This approach is particularly useful for larger dimension correlation matrices where more near-degenerate energy states can appear in the spectrum.

DOI: 10.1103/PhysRevD.87.094506 PACS numbers: 11.15.Ha, 12.38.−t, 12.38.Gc

I. INTRODUCTION

Resonances represent some of the rich dynamics of one of the fundamental interactions of Nature, the strong interaction of quarks and gluons. Lattice QCD is the only ab initio first principles approach to the fundamental quantum field theory governing the properties of hadrons and ultimately we wish to test our theoretical understanding of resonances against their experimentally determined properties.

From lattice QCD, the ground-state hadron spectrum is now relatively well understood [1]. However, gaining knowledge of the excited-state spectrum on the lattice presents additional challenges, as the excited energy states are extracted from the sub-leading exponentials of the correlation functions. A determination of the excited state energy spectrum, including multiparticle states, requires significant effort and some progress is now being made. We can expect the interplay between lattice QCD predictions and experimental measurement to be very productive in the coming years.

In the case of nucleon resonances, the first positive parity excitation of the nucleon, the $N\frac{1}{2}^{+}(1440)\mathrm{P}_{11}$ or Roper resonance, has been a subject of considerable interest since its discovery in 1964 through a partial-wave analysis of pion-nucleon scattering data [2]. This state has a surprisingly low mass, which is well below the first negative parity excitation. In constituent quark models with a harmonic oscillator potential this P_{11} state (with principal quantum number $N = 2$) appears above the lowest-lying odd-parity S_{11} (1535) state [3,4], whereas in Nature the Roper resonance is almost 100 MeV below the S_{11} state. This presents a phenomenological challenge to our understanding of level ordering. Similar difficulties occur with the $J^P = \frac{3}{2}^{+}\,\Delta^*(1600)$ and $\frac{1}{2}^{+}\,\Sigma^*(1690)$ resonances. Due to its surprisingly low mass, the P_{11} state has lead to enormous curiosity and much speculation about its nature. For example, the Roper resonance has been described as a hybrid baryon with explicitly excited gluon field configurations [5,6], or as a breathing mode of the ground state [7] or as a five quark (meson-baryon) state [8]. Significant resources have been devoted in the past from the lattice QCD perspective to find the elusive low-lying Roper state, in both quenched [9–25] and in full [26–30] QCD.

The 'Variational method' [31,32] is the state-of-the-art approach for determining the excited state hadron spectrum. It is based on the creation of a matrix of correlation functions in which different superpositions of excited-state contributions are linearly combined to isolate the energy eigenstates. A low-lying Roper state was identified with this method using a variety of source and sink smearings in constructing correlation matrices [22,24] in quenched QCD. Recent developments of algorithms and computational power have enabled the extension to full QCD. Some full QCD analyzes using the variational method can be found in Refs. [26–29,33–39]. Here we consider the techniques of Refs. [22,24] to explore the low-lying even- and odd- parity states of the nucleon using $2 + 1$-flavor dynamical QCD gauge-field configurations from the PACS-CS collaboration [40]. A small subset of the results presented here have appeared in Refs. [29,41].

The number of energy states revealed in the correlation matrix method depends on the number of unique operators chosen which have the quantum numbers of the desired states. Hence, a clear identification of these states is necessary to observe changes in these energy states as a function of quark mass, in principle to the physical quark mass. This allows the quark mass dependence and structure of the extracted energy eigenstates to be explored systematically. The new technique that we develop here can be used when any parameter of the theory is varied to explore how the nature of the states and energies change with that parameter.

The principal focus of this paper is to present the details of our eigenvector analysis to track the states from the heavy to the light quark mass region. In doing so, we consider the $N^{\pm}$ states to illustrate the utility of the

method. The operator basis is increased with the use of fermion source and sink smearings as in Ref. [29]. Then, the propagation of the energy states are presented after analyzing the state of eigenvectors at adjacent quarks masses. Results are presented for both the nonsymmetric and symmetric eigenvalue equations, and these are compared and related to each other.

In this analysis, we haven't been able to isolate the multiparticle thresholds at our three light quark masses. We proceed under the assumption that the couplings to these 5+ quark states have relatively small overlap with our 3-quark interpolators and that the effective mass functions are largely unaffected by multiparticle states with small couplings to our interpolators. To monitor this we use the full covariance-matrix based χ^2/dof in order to accurately assess the extent to which our effective mass function plateau is associated with a single state. Ultimately, in addition to the 3-quark operators, one needs to include 5- or 7- or more- quark operators [35,42,43] in the correlation matrix to extract all the states in the spectrum.

If we denote the dimensionality of the Hilbert space of the lattice Hamiltonian to be N, then in an ideal world we would select N linearly independent operators to construct our $N \times N$ correlation matrix with sufficient statistical accuracy and then diagonalize this to obtain the exact N energy eigenstates for this lattice Hamiltonian. Obviously and unfortunately, this is not computationally feasible on any realistic lattice, and the best that we can do is choose a relatively small number of operators, M, where $M \ll N$. If we choose these M operator interpolating fields wisely, then the subspace they span will have good overlap with the subspace spanned by the M lowest eigenstates of the Hamiltonian. If this is the case, with sufficient statistics we can hope to extract good estimates of the M lowest energy states. If we observe, for example, that adding additional operators to increase M to M' reveals new low-lying states, then clearly we had not chosen our M operators wisely enough. The test of whether or not we have revealed all of the lowest states of the lattice Hamiltonian is that the process of adding additional and new operators does not reveal new low-lying excited states. We present a clearer and more complete discussion of these issues in the Appendix.

The linear independence of additional operators can be judged by monitoring the condition number of the correlation matrix. If the condition number does not increase significantly when an operator is added then the additional operator enhances the basis in a sufficiently independent manner.

The paper is arranged as follows: Section II contains a standard description of the mass extraction from a two-point correlation function with a brief introduction of Gaussian smearings at the fermion sources. The variational method is presented in Sec. III, followed by simulation details in Sec. IV. Section V contains a discussion of the energy eigenstates identification. Results for the flow of eigenvectors are presented in Sec. VI, followed by concluding remarks in Sec. VII. Finally, a pedagogical discussion of the correlation matrix is presented in Appendix in terms of the lattice Hamiltonian.

II. ENERGY STATES FROM TWO-POINT CORRELATION FUNCTIONS

A two point correlation function can be written as

$$G_{ij}(t, \vec{p}) = \sum_{\vec{x}} e^{-i\vec{p}.\vec{x}} \langle \Omega | T\{\chi_i(x) \bar{\chi}_j(0)\} | \Omega \rangle, \tag{1}$$

where the Dirac spin indices are implicit. The operator $\bar{\chi}_j(0)$ creates states from the vacuum at space-time point 0 and, following the evolution of the states in Euclidean time t, the states are destroyed by the operator $\chi_i(x)$ at the point $(\vec{x}, t)$. T indicates the time ordering of the operators.

The energy eigenstates of hadrons are extracted using operators suitably chosen to have overlap with the desired states of interest. If we consider a baryon state B, then a complete set of momentum eigenstates provides,

$$\sum_{B,\vec{p}',s} |B, \vec{p}', s\rangle \langle B, \vec{p}', s| = I, \tag{2}$$

where B can also include multiparticle states that the operator χ couples with. The substitution of Eq. (2) into Eq. (1) yields

$$G_{ij}(t, \vec{p}) = \sum_{\vec{x}} \sum_{B,\vec{p}',s} e^{-i\vec{p}.\vec{x}} \langle \Omega | \chi_i(x) | B, \vec{p}', s\rangle \times \langle B, \vec{p}', s | \bar{\chi}_j(0) | \Omega \rangle. \tag{3}$$

Using the translational operator, the operator $\chi_i(x)$ can be expressed as

$$\chi_i(x) = e^{Ht} e^{-i\vec{P}\cdot\vec{x}} \chi_i(0) e^{i\vec{P}\cdot\vec{x}} e^{-Ht}, \tag{4}$$

where H is the lattice Hamiltonian and $\vec{P}$ is the momentum operator whose eigenvalue is the total momentum $\vec{p}$ of the system. Inserting this into Eq. (3) we obtain

$$\begin{aligned} G_{ij}(t, \vec{p}) &= \sum_{\vec{x}} \sum_{B,\vec{p}',s} e^{-E_B t} e^{-i\vec{x}.(\vec{p}-\vec{p}')} \langle \Omega | \chi_i(0) | B, \vec{p}', s\rangle \\ &\quad \times \langle B, \vec{p}', s | \bar{\chi}_j(0) | \Omega \rangle \\ &= \sum_{B,\vec{p}',s} e^{-E_B t} \delta_{\vec{p},\vec{p}'} \langle \Omega | \chi_i(0) | B, \vec{p}', s\rangle \\ &\quad \times \langle B, \vec{p}', s | \bar{\chi}_j(0) | \Omega \rangle \\ &= \sum_{B} \sum_{s} e^{-E_B t} \langle \Omega | \chi_i(0) | B, \vec{p}, s\rangle \langle B, \vec{p}, s | \bar{\chi}_j(0) | \Omega \rangle. \end{aligned} \tag{5}$$

The overlap of the interpolating fields $\chi(0)$ and $\bar{\chi}(0)$ with positive and negative parity baryon states $|B^{\pm}\rangle$ can be parametrized by a complex quantity called the coupling

strength, $\lambda_{B^\pm}$, which can be defined for positive parity states by

$$\langle\Omega|\chi(0)|B^+,\vec{p},s\rangle = \lambda_{B^+}\sqrt{\frac{M_{B^+}}{E_{B^+}}}u_{B^+}(\vec{p},s), \tag{6}$$

$$\langle B^+,\vec{p},s|\bar{\chi}(0)|\Omega\rangle = \bar{\lambda}_{B^+}\sqrt{\frac{M_{B^+}}{E_{B^+}}}\bar{u}_{B^+}(\vec{p},s). \tag{7}$$

For the negative parity states one requires

$$\langle\Omega|\chi(0)|B^-,\vec{p},s\rangle = \lambda_{B^-}\sqrt{\frac{M_{B^-}}{E_{B^-}}}\gamma_5 u_{B^-}(\vec{p},s), \tag{8}$$

$$\langle B^-,\vec{p},s|\bar{\chi}(0)|\Omega\rangle = -\bar{\lambda}_{B^-}\sqrt{\frac{M_{B^-}}{E_{B^-}}}\bar{u}_{B^-}(\vec{p},s)\gamma_5. \tag{9}$$

Here, $\lambda_{B^\pm}$ and $\bar{\lambda}_{B^\pm}$ are the couplings of the interpolating functions at the sink and the source, respectively, and $M_{B^\pm}$ is the mass of the state $B^\pm$. $E_{B^\pm}$ is the energy of the state $B^\pm$, where $E_{B^\pm} = \sqrt{M_{B^\pm}^2 + \vec{p}^2}$. Therefore, mass of a energy state is obtained with the momentum projection of the correlation function at $\vec{p} = 0$.

The standard spin sums may now be performed. For the positive parity hadron states, this can be expressed as

$$\sum_s u^\beta_{B^+}(\vec{p},s)\bar{u}^\alpha_{B^+}(\vec{p},s) = \frac{\gamma.p + M_{B^+}}{2M_{B^+}}, \tag{10}$$

and for the negative parity states, one encounters

$$-\gamma_5\Big(\sum_s u^\beta_{B^-}(\vec{p},s)\bar{u}^\alpha_{B^-}(\vec{p},s)\Big)\gamma_5 = \frac{+\gamma.p - M_{B^-}}{2M_{B^-}}. \tag{11}$$

By substituting the above Eqs. for the positive and negative parity states in Eq. (5) we obtain,

$$\mathcal{G}_{ij}(t,\vec{p}) = \sum_{B^+}\lambda_{B^+}\bar{\lambda}_{B^+}e^{-E_{B^+}t}\frac{\gamma.p_{B^+} + M_{B^+}}{2E_{B^+}} + \sum_{B^-}\lambda_{B^-}\bar{\lambda}_{B^-}e^{-E_{B^-}t}\frac{+\gamma.p_{B^-} - M_{B^-}}{2E_{B^-}}. \tag{12}$$

At momentum $\vec{p} = \vec{0}$, $E_{B^\pm} = M_{B^\pm}$, and a parity projection operator $\Gamma_\pm$ can be introduced,

$$\Gamma_\pm = \frac{1}{2}(\gamma_0 \pm 1). \tag{13}$$

We can isolate the masses of the even and odd parity energy states by taking the trace of $\mathcal{G}$ with the operators Γ_+ and Γ_-. The positive parity states propagate through the (1, 1) and (2, 2) elements of the Dirac matrix, whereas, negative parity states propagate through the (3, 3) and (4, 4) elements. The correlation function for positive and negative parity states can then be written as

$$G^\pm_{ij}(t,\vec{0}) = \mathrm{Tr}_{\mathrm{sp}}[\Gamma_\pm\mathcal{G}_{ij}(t,\vec{0})] = \sum_{B^\pm}\lambda^\pm_i\bar{\lambda}^\pm_j e^{-M_{B^\pm}t}. \tag{14}$$

The correlation function contains a superposition of energy states, i.e., both ground and excited energy states. The mass of the lowest energy state, $M_{0^\pm}$ can be extracted at large t where the contributions from all other excited states are suppressed,

$$G^\pm_{ij}(t,\vec{0}) \overset{t\to\infty}{=} \lambda^\pm_{i0}\bar{\lambda}^\pm_{j0}e^{-M_{0^\pm}t}, \tag{15}$$

where, $\lambda^\pm_{i0}$ and $\bar{\lambda}^\pm_{j0}$ are now couplings of interpolators to the lowest energy state.

A. Source smearing

The spatial fermion source-smearing [44] technique is applied to increase the overlap of the interpolators with the lower lying states. We employ a fixed boundary condition in the time direction for the fermions by setting $U_t(\vec{x},N_t) = 0\ \forall\ \vec{x}$ in the hopping terms of the fermion action with periodic boundary conditions imposed in the spatial directions. Gauge invariant Gaussian smearing [44] in the spatial dimensions is applied through an iterative process. The smearing procedure is:

$$\psi_i(\vec{x},t) = \sum_{x'}F(\vec{x},\vec{x}')\psi_{i-1}(\vec{x}',t), \tag{16}$$

where,

$$F(\vec{x},\vec{x}') = (1-\alpha)\delta_{x,x'} + \frac{\alpha}{6}\sum_{\mu=1}^{3}[U_\mu(x)\delta_{x',x+\hat{\mu}} + U^\dagger_\mu(x-\hat{\mu})\delta_{x',x-\hat{\mu}}], \tag{17}$$

where the parameter $\alpha = 0.7$ is used in our calculation. After repeating the procedures N_{sm} times on a point source the resulting smeared fermion field is,

$$\psi_{N_{\mathrm{sm}}}(\vec{x},t) = \sum_{x'}F^{N_{sm}}(\vec{x},\vec{x}')\psi_0(\vec{x}',t). \tag{18}$$

III. VARIATIONAL METHOD

The extraction of the ground state mass can be done straightforwardly using Eq. (15). However access to the excited state masses requires additional effort due to the presence of these energy states at the subleading of the exponential. Here we consider the variational method [31,32], which allows for a variety of superpositions of excited-states in its cross correlation discussed below.

The variational method requires the cross correlation of operators so that the operator space can be diagonalized and the excited state masses extracted from the exponential nature of the diagonalized basis. To access N states of the spectrum, one requires a minimum of N interpolators. With the assumption that only N states contribute significantly to

G_{ij} at time t, the parity projected two point correlation function matrix for $\vec{p} = 0$ can be written as

$$G^{\pm}_{ij}(t) \equiv G^{\pm}_{ij}(t,\vec{0}) = \left(\sum_{\vec{x}} \mathrm{Tr}_{\mathrm{sp}}\{\Gamma_{\pm}\langle\Omega|\chi_i(x)\bar{\chi}_j(0)|\Omega\rangle\}\right) = \sum_{\alpha=0}^{N-1} \lambda^{\alpha}_i \bar{\lambda}^{\alpha}_j e^{-m_\alpha t}, \tag{19}$$

where Dirac indices are implicit. Here, λ^{α}_i and $\bar{\lambda}^{\alpha}_j$ are the couplings of interpolators χ_i and $\bar{\chi}_j$ at the sink and source, respectively, to eigenstates $\alpha = 0, \ldots, (N-1)$ and m_α is the mass of the energy state α. The use of identical source and sink interpolators provides $\bar{\lambda}^{\alpha}_j = (\lambda^{\alpha}_j)^*$ and then in the ensemble average $G^{\pm}_{ij}(t)$ is a Hermitian matrix, i.e., $G^{\pm}_{ij}(t) = [G^{\pm}_{ji}(t)]^*$. Moreover, considering both $\{U\}$ and $\{U^*\}$ configurations makes $G^{\pm}_{ij}(t)$ a real symmetric matrix. The N interpolators have the same quantum numbers and provide an N-dimensional basis upon which to describe the states. Using this basis we aim to construct N independent interpolating source and sink fields which isolate N baryon states $|B_\alpha\rangle$, i.e.,

$$\bar{\phi}^{\,\alpha} = \sum_{i=1}^{N} u^{\alpha}_i \bar{\chi}_i, \tag{20}$$

$$\phi^{\alpha} = \sum_{i=1}^{N} v^{\alpha}_i \chi_i, \tag{21}$$

such that,

$$\langle B_\beta, p, s|\bar{\phi}^{\alpha}|\Omega\rangle = \delta_{\alpha\beta}\bar{z}^{\alpha}\bar{u}(\alpha, p, s), \tag{22}$$

$$\langle\Omega|\phi^{\alpha}|B_\beta, p, s\rangle = \delta_{\alpha\beta}z^{\alpha}u(\alpha, p, s), \tag{23}$$

where z^α and $\bar{z}^\alpha$ are the coupling strengths of ϕ^α and $\bar{\phi}^\alpha$ to the state $|B_\alpha\rangle$. Consider a real eigenvector u^{α}_j which operates on the correlation matrix $G_{ij}(t)$ from the right, one can obtain

$$G_{ij}(t)u^{\alpha}_j = \left(\sum_{\vec{x}} \mathrm{Tr}_{\mathrm{sp}}\{\Gamma_{\pm}\langle\Omega|\chi_i\bar{\chi}_j|\Omega\rangle\}\right)u^{\alpha}_j = \lambda^{\alpha}_i\bar{z}^{\alpha}e^{-m_\alpha t}. \tag{24}$$

For notational convenience, in the remainder of the discussion the repeated indices i, j, k are to be understood as being summed over, whereas, α, which stands for a particular state, is not.

In the ensemble average, $G_{ij}(t) = G_{ji}(t)$. Therefore, considering $\frac{1}{2}[G_{ij}(t) + G_{ji}(t)]$ provides an improved unbiased estimator and enables the use a symmetric eigenvalue equation as discussed below. To ensure that the matrix elements are all $\sim\mathcal{O}(1)$, each element of $G_{ij}(t)$ is normalized by $\frac{1}{\sqrt{G_{ii}(0)}}G_{ij}(t)\frac{1}{\sqrt{G_{jj}(0)}}$ (discussed in the Appendix).

In Eq. (24), since the only t dependence comes from the exponential term, we can write a recurrence relation at time $(t_0 + \Delta t)$ as

$$G_{ij}(t_0 + \triangle t)u^{\alpha}_j = e^{-m_\alpha \triangle t}G_{ij}(t_0)u^{\alpha}_j \tag{25}$$

for sufficiently large t_0 and $t_0 + \Delta t$ [21,45].

Multiplying the above equation by $[G_{ij}(t_0)]^{-1}$ from the left we get,

$$[(G(t_0))^{-1}G(t_0 + \Delta t)]u^{\alpha} = e^{-m_\alpha \Delta t}u^{\alpha} = c^{\alpha}u^{\alpha}. \tag{26}$$

This is an eigenvalue equation for eigenvector u^α with eigenvalue $c^\alpha = e^{-m_\alpha\Delta t}$. We can also solve the left eigenvalue equation to recover the v^α eigenvector,

$$v^{\alpha}_i G_{ij}(t_0 + \triangle t) = e^{-m_\alpha \Delta t}v^{\alpha}_i G_{ij}(t_0). \tag{27}$$

Similarly,

$$v^{\alpha}[G(t_0 + \Delta t)(G(t_0))^{-1}] = e^{-m_\alpha \Delta t}v^{\alpha}. \tag{28}$$

Since $G_{ij}(t)$ is a real symmetric matrix $v = u$. The vectors u^{α}_j and v^{α}_i diagonalize the correlation matrix at time t_0 and $t_0 + \Delta t$ making the projected correlation matrix,

$$v^{\alpha}_i G_{ij}(t)u^{\beta}_j = \delta^{\alpha\beta}z^{\alpha}\bar{z}^{\beta}e^{-m_\alpha t}. \tag{29}$$

The parity-projected, eigenstate-projected correlator,

$$v^{\alpha}_i G^{\pm}_{ij}(t)u^{\alpha}_j \equiv G^{\alpha}_{\pm,} \tag{30}$$

is then used to obtain masses of different states. We construct the effective mass function

$$M^{\alpha}_{\mathrm{eff}}(t) = \ln\left(\frac{G^{\alpha}_{\pm}(t,\vec{0})}{G^{\alpha}_{\pm}(t+1,\vec{0})}\right) = M^{\alpha}_{\pm} \tag{31}$$

and apply standard analysis techniques as described in Ref. [21].

Since $G(t_0)^{-1/2}G(t_0)^{1/2} = I$, we can rewrite Eq. (26) as

$$G(t_0)^{-1}G(t_0 + \Delta t)G(t_0)^{-1/2}G(t_0)^{1/2}u^{\alpha} = c^{\alpha}u^{\alpha}.$$

Multiplying from the left by $G(t_0)^{1/2}$ provides

$$G(t_0)^{-1/2}G(t_0 + \Delta t)G(t_0)^{-1/2}G(t_0)^{1/2}u^{\alpha} = c^{\alpha}G(t_0)^{1/2}u^{\alpha}$$

and defining,

$$w^{\alpha} = G(t_0)^{1/2}u^{\alpha} \tag{32}$$

we find

$$G(t_0)^{-1/2}G(t_0 + \Delta t)G(t_0)^{-1/2}w^{\alpha} = c^{\alpha}w^{\alpha} \tag{33}$$

(also shown in Eq. (A8)). We note the matrix

$$[G(t_0)^{-1/2}G(t_0 + \triangle t)G(t_0)^{-1/2}] \tag{34}$$

is real symmetric, with the same eigenvalue c^α and with the $\vec{w}^\alpha$ orthogonal to each other. If we had not used the $[U + U^*]$ sum then the matrix in Eq. (34)

would be Hermitian and hence would still have real eigenvalues and orthogonal eigenvectors. The coefficients of interpolators creating an energy eigenstate is recovered by

$$u^{\alpha} = G(t_0)^{-1/2} w^{\alpha}. \tag{35}$$

IV. SIMULATION PARAMETERS

PACS-CS $2+1$ flavor dynamical-fermion configurations [40] made available through the ILDG [46] are used. These configurations use the nonperturbatively $\mathcal{O}(a)$-improved Wilson fermion action and the Iwasaki-gauge action [47]. The lattice volume is $32^3 \times 64$, with $\beta = 1.90$ providing a lattice spacing $a = 0.0907$ fm and lattice volume of $\approx (2.90\ \text{fm})^3$.

The degenerate up and down quark masses are considered, with the hopping parameter values of $\kappa_{ud} = 0.13700$, 0.13727, 0.13754, 0.13770 and 0.13781 corresponding to pion masses of $m_\pi = 0.702$, 0.572, 0.413, 0.293, 0.156 GeV [40]; for the strange quark $\kappa_s = 0.13640$. We consider an ensemble of 350 configurations each for the four heavier quarks mass and 198 configurations for the lightest quark. An ensemble of 750 samples for the lightest quark mass is created by using well separated multiple fermion sources on each configuration. We use the jackknife method to calculate the error, where the χ^2/dof for projected correlator fits is obtained via a covariance matrix analysis.

The complete set of local interpolating fields for the spin-$\frac{1}{2}$ nucleon are considered herein. Three different spin-flavor combinations of nucleon interpolators are considered,

$$\chi_1(x) = \epsilon^{abc}(u^{Ta}(x) C\gamma_5 d^b(x)) u^c(x), \tag{36}$$

$$\chi_2(x) = \epsilon^{abc}(u^{Ta}(x) C d^b(x)) \gamma_5 u^c(x), \tag{37}$$

$$\chi_4(x) = \epsilon^{abc}(u^{Ta}(x) C\gamma_5\gamma_4 d^b(x)) u^c(x). \tag{38}$$

The χ_1 and χ_2 interpolators are used in Refs. [12,48,49]. The interpolator χ_4 is the time component of the local spin-$\frac{3}{2}$ isospin-$\frac{1}{2}$ interpolator which also couples to spin-$\frac{1}{2}$ states used, for instance, in Refs. [16,21,50].

The local scalar-diquark nucleon interpolator, χ_1, is well known to have a good overlap with the ground state of the nucleon. Also, this χ_1 interpolator is able to extract a low-lying Roper state in quenched QCD [24]. On the other hand, the χ_2 interpolator has pseudoscalar-diquark structure in the nucleon, which vanishes in the nonrelativistic limit, couples strongly to higher energy states. Each interpolator has a unique Dirac structure giving rise to different spin-flavor combinations. Moreover, as each spinor has upper and lower components, with the lower components containing an implicit derivative, different combinations of zero, one, two and three derivative interpolators are provided.

The correlation matrices are constructed using different levels of gauge-invariant Gaussian smearing [44] at the fermion sources and sinks [29]. A basis of smearing-sweep counts of 16, 35, 100 and 200 is selected following the extensive analysis of Ref. [29].

It is important to consider the condition number for these matrices in order to examine the quality of our operator basis. We consider the normalized correlation matrix, $G_{ij}(t)/(G_{ii}(t)G_{jj}(t))^{-1/2}$, with $G_{ij}(t)$ made Hermitian as discussed in Sec. III.

The condition numbers for our correlation matrices are illustrated in Fig. 1. We examine the change in the condition number for matrices composed of χ_1 and χ_2 as additional source smearings are introduced. We consider two levels of smearing in the 4×4 matrix, three levels of smearing in the 6×6 matrix and all four levels of smearing in the 8×8 matrix.

Results for the five quark masses under consideration are provided. The tight clustering of the condition number for the wide range of quark masses considered indicates that the basis selected is appropriate for all these masses.

The condition numbers are displayed as a function of Euclidean time following the fermion source at $t_s = 16$. At early times, the different superposition of large excited state contributions gives rise to a relatively small condition number. However as these states become exponentially suppressed at larger Euclidean times, the condition number increases. If one waits to very large Euclidean times, all excitations are suppressed and all operators produce the same ground state rendering the condition number infinite. This will be realized for any basis set having overlap with the ground state. Thus it is important to conduct the correlation matrix analysis at times where excited states are

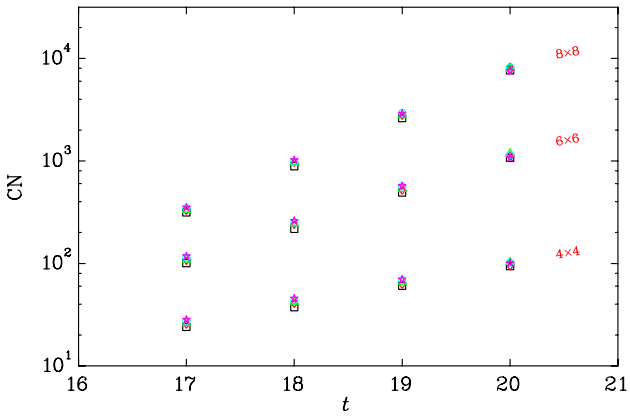

FIG. 1 (color online). The condition numbers, CN, of 4×4, 6×6 and 8×8 correlation matrices using χ_1 and χ_2 operators, are illustrated as a function of Euclidean time, t. The 4×4 matrix includes 200 and 100 sweeps, 6×6 contains 200, 100 and 35 sweeps and 8×8 incorporates all four sources, 200, 100, 35 and 16 sweeps. Each cluster of points contains five values corresponding to the five quark masses considered.

present and the number of significant state contributions matches the size of the basis.

While the condition number increases as the smearing basis is enhanced, the condition number is the order of 10^3 for our preferred variational analysis time of $t_0 = 18$. This value is small relative to 10^{12} associated with standard double precision calculations.

Thus, the utilization of different fermion smearings at the source and the sink is an effective approach to enlarging the basis of operators. Our selection of smearing levels was based on the excited-state contributions observed in smeared-source to point-sink correlators [29]. By selecting smearing levels that provided well separated effective masses at early Euclidean times, we ensured that each operator was sufficiently independent, thus giving rise to an acceptable condition number for the correlation matrix.

V. EIGENSTATES IDENTIFICATION

Let us consider M interpolating fields making an $M \times M$ parity-projected correlation matrix $G(t)$. In solving the generalized eigenvalue equations of Eqs. (26) and (28) we encounter the real and approximately symmetric matrices $[(G(t_0))^{-1}G(t_0 + \Delta t)]$ and $[G(t_0 + \Delta t)(G(t_0))^{-1}]$, with the left and right eigenvectors $\vec{u}^{\alpha}$ and $\vec{v}^{\alpha}$, respectively. Thus the eigenvectors of these matrices are expected to be approximately orthogonal (left table in Table I). As explained in the Appendix, the reason we have only approximate symmetry is that $G(t)$ does not commute with itself at different times. This results because $M < N$. The more closely the subspace spanned by our M operators aligns with the subspace of the lowest M energy eigenstates of H, the less violation of symmetry there will be. If we do not use the $[U + U^*]$ sum, then all of the same arguments hold but with Hermitian matrices.

This feature enables the use of the generalized measure

$$\mathcal{U}^{\alpha\beta}(m_q, m_{q'}) = \vec{u}^{\alpha}(m_q) \cdot \vec{u}^{\beta}(m_{q'}) \tag{39}$$

for the eigenvector $\vec{u}^{\alpha}$, for example. This correlates eigenvectors at different quark masses and may be useful in tracking states.

In contrast, as already discussed, the matrix in Eq. (34) is symmetric, hence the eigenvectors $\vec{w}^{\alpha}(m_q)$ are exactly orthogonal, i.e., $\vec{w}^{\alpha}(m_q) \cdot \vec{w}^{\beta}(m_q) = \delta_{\alpha\beta}$ (right table in Table I).

Therefore, as in Eq. (39), a generalized measure

$$\mathcal{W}^{\alpha\beta}(m_q, m_{q'}) = \vec{w}^{\alpha}(m_q) \cdot \vec{w}^{\beta}(m_{q'}) \tag{40}$$

for the $\vec{w}^{\alpha}$ can be constructed to identify the states more reliably as we move from quark mass m_q to the adjacent quark mass $m_{q'}$.

In Table II, the generalized measures $\mathcal{U}^{\alpha\beta}(m_q, m_{q'})$ and $\mathcal{W}^{\alpha\beta}(m_q, m_{q'})$ are presented for the heaviest and the second heaviest quark masses. It is evident that the off-diagonal elements of $\mathcal{W}^{\alpha\beta}(m_q, m_{q'})$ are smaller than the $\mathcal{U}^{\alpha\beta}(m_q, m_{q'})$ and hence will be more reliable for identification and tracking of the energy eigenstates. Therefore we use $\mathcal{W}^{\alpha\beta}(m_q, m_{q'})$ for this purpose. For each value of α

TABLE I. The scalar product $\vec{u}^{\alpha}(m_q) \cdot \vec{u}^{\beta}(m_q)$ (left) and $\vec{w}^{\alpha}(m_q) \cdot \vec{w}^{\beta}(m_q)$ (right), for the same quark mass, with four different levels of smearings. States are ordered from left to right and top to bottom in order of increasing excited-state mass. α and β correspond to row and column, respectively.

1.00	−0.18	0.02	−0.07	0.65	0.10	−0.32	−0.09	**1.00**	0.00	0.00	0.00	0.00	0.00	0.00	0.00
−0.18	**1.00**	0.02	0.36	−0.10	−0.49	0.06	0.39	0.00	**1.00**	0.00	0.00	0.00	0.00	0.00	0.00
0.02	0.02	**1.00**	0.15	0.07	0.06	0.42	0.03	0.00	0.00	**1.00**	0.00	0.00	0.00	0.00	0.00
−0.07	0.36	0.15	**1.00**	−0.03	0.23	0.09	0.30	0.00	0.00	0.00	**1.00**	0.00	0.00	0.00	0.00
0.65	−0.10	0.07	−0.03	**1.00**	0.15	−0.57	−0.13	0.00	0.00	0.00	0.00	**1.00**	0.00	0.00	0.00
0.10	−0.49	0.06	0.23	0.15	**1.00**	−0.06	−0.61	0.00	0.00	0.00	0.00	0.00	**1.00**	0.00	0.00
−0.32	0.06	0.42	0.09	−0.57	−0.06	**1.00**	0.17	0.00	0.00	0.00	0.00	0.00	0.00	**1.00**	0.00
−0.09	0.39	0.03	0.30	−0.13	−0.61	0.17	**1.00**	0.00	0.00	0.00	0.00	0.00	0.00	0.00	**1.00**

TABLE II. The scalàr product $\vec{u}^{\alpha}(m_q) \cdot \vec{u}^{\beta}(m_{q'})$ (left) and $\vec{w}^{\alpha}(m_q) \cdot \vec{w}^{\beta}(m_{q'})$ (right), for $\kappa = 0.13700$ and $\kappa' = 0.13727$, with four different levels of smearings. States are ordered from left to right for $m_{q'}$ and top to bottom for m_q in order of increasing excited-state mass. α and β correspond to row and column, respectively.

0.98	−0.29	−0.14	0.63	−0.07	0.10	−0.32	−0.08	**1.00**	−0.09	0.00	0.00	0.01	0.00	0.01	0.00
−0.19	**−0.92**	0.08	−0.03	0.14	0.06	0.42	0.05	0.09	**0.99**	−0.07	0.13	−0.01	0.00	0.01	0.00
−0.16	0.07	**0.99**	−0.09	−0.04	−0.53	0.09	0.36	0.01	0.07	**1.00**	−0.01	0.00	−0.01	0.00	0.00
0.63	−0.44	−0.02	**0.99**	−0.05	0.13	−0.55	−0.12	−0.01	−0.13	0.02	**0.98**	−0.09	0.02	0.07	0.00
−0.12	−0.11	0.40	0.00	**0.75**	0.00	0.08	0.36	0.01	0.01	0.00	−0.09	**−0.97**	0.21	−0.01	0.03
0.05	−0.11	−0.42	0.17	0.76	**0.95**	−0.12	−0.53	0.00	0.00	0.01	0.00	0.20	**0.95**	−0.07	−0.23
−0.45	−0.17	0.03	−0.67	0.08	−0.05	**1.00**	0.18	−0.01	0.00	0.00	−0.07	0.01	0.07	**0.99**	−0.01
−0.09	0.00	0.34	−0.14	−0.34	−0.82	0.21	**1.00**	0.00	0.00	0.00	−0.01	−0.08	−0.21	0.01	**−0.97**

TABLE III. The scalar product $\vec{w}^{\alpha}(m_q) \cdot \vec{w}^{\beta}(m_{q'})$, for $\kappa = 0.13700$ ($m_\pi = 702$ MeV) and $\kappa' = 0.13727$ ($m_\pi = 572$ MeV) (top left), $\kappa = 0.13727$ ($m_\pi = 572$ MeV) and $\kappa' = 0.13754$ ($m_\pi = 402$ MeV) (top right), $\kappa = 0.13754$ ($m_\pi = 402$ MeV) and $\kappa' = 0.13770$ ($m_\pi = 293$ MeV) (bottom left), $\kappa = 0.13770$ ($m_\pi = 293$ MeV) and $\kappa' = 0.13781$ ($m_\pi = 156$ MeV) (bottom right), for an 8×8 correlation matrix of χ_1 and χ_2, with four different levels of smearings. States are ordered from left to right for $m_{q'}$ and top to bottom for m_q in order of increasing excited-state mass. α and β correspond to row and column, respectively.

1.00	−0.09	0.00	0.00	0.01	0.00	0.01	0.00	**1.00**	−0.08	0.01	−0.01	0.01	0.01	0.00	0.00
0.09	**0.99**	−0.07	0.13	−0.01	0.00	0.01	0.00	0.08	**0.98**	0.12	−0.03	0.09	0.01	0.00	0.00
0.01	0.07	**1.00**	−0.01	0.00	−0.01	0.00	0.00	−0.02	−0.12	**0.99**	−0.08	0.00	0.00	0.00	−0.01
−0.01	−0.13	0.02	**0.98**	−0.09	0.02	0.07	0.00	−0.01	−0.09	−0.01	0.03	**0.99**	−0.10	0.00	0.00
0.01	0.01	0.00	−0.09	**−0.97**	0.21	−0.01	0.03	0.01	0.02	0.08	**0.99**	−0.02	0.01	0.07	0.05
0.00	0.00	0.01	0.00	0.20	**0.95**	−0.07	−0.23	0.00	0.00	−0.01	−0.08	0.00	−0.08	**0.99**	0.07
−0.01	0.00	0.00	−0.07	0.01	0.07	**0.99**	−0.01	0.01	0.02	0.00	0.01	−0.10	**−0.99**	−0.08	0.03
0.00	0.00	0.00	−0.01	−0.08	−0.21	0.01	**−0.97**	0.00	0.00	0.00	−0.04	0.00	0.03	−0.08	**1.00**
1.00	−0.04	−0.02	0.04	0.01	0.00	0.00	0.00	**1.00**	−0.04	0.03	−0.02	0.01	0.00	0.01	0.00
0.03	**0.98**	−0.21	0.04	−0.01	0.00	−0.03	0.00	0.03	**0.97**	0.25	0.06	−0.02	−0.01	−0.01	−0.01
0.02	0.21	**0.97**	0.01	0.14	0.04	−0.02	−0.04	−0.03	−0.24	**0.94**	−0.07	−0.21	0.00	−0.03	−0.02
0.01	−0.01	−0.13	−0.37	**0.92**	0.08	−0.03	−0.03	0.02	−0.06	−0.03	**0.93**	−0.36	−0.06	0.02	0.00
−0.04	−0.04	−0.05	**0.93**	0.36	0.02	0.00	−0.01	−0.01	−0.05	0.20	0.35	**0.89**	−0.03	−0.21	−0.01
0.00	−0.03	−0.01	0.01	−0.01	−0.25	**−0.97**	−0.03	−0.01	−0.01	0.06	0.04	0.18	−0.23	**0.93**	−0.20
0.00	−0.01	−0.04	0.01	−0.10	**0.95**	−0.24	−0.16	0.01	0.00	−0.02	−0.08	−0.04	**−0.97**	−0.22	0.05
0.00	−0.01	−0.02	0.00	−0.02	−0.15	0.07	**−0.99**	0.01	0.00	−0.04	−0.02	−0.04	0.00	−0.20	**−0.98**

there is only one value for β where the entry is within a few percent of 1. Thus this measure provides a clear identification of how eigenvectors in the hadron spectrum at quark mass m_q are associated with eigenvectors at the next value of quark mass, $m_{q'}$.

Now we explain how we track the energy eigenstates from one quark mass to the next. Firstly, we label the extracted energy states at the heaviest quark mass with a chosen set of symbols (most right column in Fig. 2), where each symbol is assigned by the corresponding eigenvectors associated with it. These symbols are carried on to the lightest quark mass by looking at $\mathcal{W}^{\alpha\beta}(m_q, m_{q'})$ for adjacent quark masses going from the heaviest to the lightest. After the energy eigenstates are labeled at the heaviest quark, we look at the scalar product $\vec{w}^{\alpha}(m_q) \cdot \vec{w}^{\beta}(m_{q'})$ for the heaviest and the second heaviest quark mass (top left of Table III). The scalar product shows that in this case all the diagonal elements are larger than the off-diagonal, meaning there is no eigenvector crossing at these two heavier quark masses. A similar scalar product for the second heaviest to the third heaviest mass (top right of Table III) shows that the fourth and fifth eigenvectors are crossed with the fifth and fourth at the third quark mass, and a similar situation for the sixth and the seventh. To illustrate our analysis in our figures we track the eigenvectors from one quark mass to the next by connecting these similar eigenvectors by lines. In Fig. 2, two lines (eigenvectors) cross at the second and the third quark mass. We then follow the above procedures for the third, fourth and fourth and fifth (the lightest) quark masses.

It is well known in quantum mechanics the energies avoid level crossings as illustrated in Fig. 3. However, when two energy levels experience an avoided level crossing, the nature of the two eigenvectors is interchanged, as shown by the dotted lines in Fig. 3. In Fig. 2, the first and second excited energy eigenstates do not experience an avoided level crossing at pion mass of 413 MeV, whereas avoided level crossings are present for the third-fourth and the fifth-sixth excited energy states. However, note that the avoided level crossings lie within

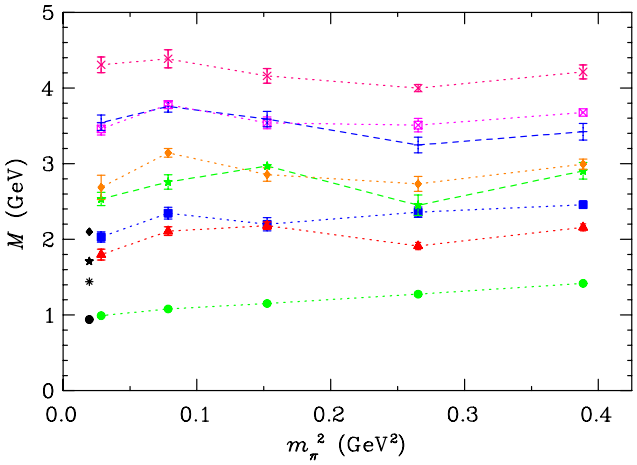

FIG. 2 (color online). $N\frac{1}{2}^{+}$ energy states from 8×8 correlation matrix of χ_1, χ_2 interpolators from $\kappa = 0.13700$ ($m_\pi = 702$ MeV, right-most column) to $\kappa = 0.13781$ ($m_\pi = 156$ MeV, left-most column). The symbols follow the eigenvector as determined by considering the scalar product $\vec{w}^{\alpha} \cdot \vec{w}^{\beta}$, as presented in Table III. Note that the dotted lines in the figure connect similar eigenvectors. Where these lines cross, of course the energy levels would not cross, but we would see an avoided level crossing as in Fig. 3 if we had data for every quark or pion mass.

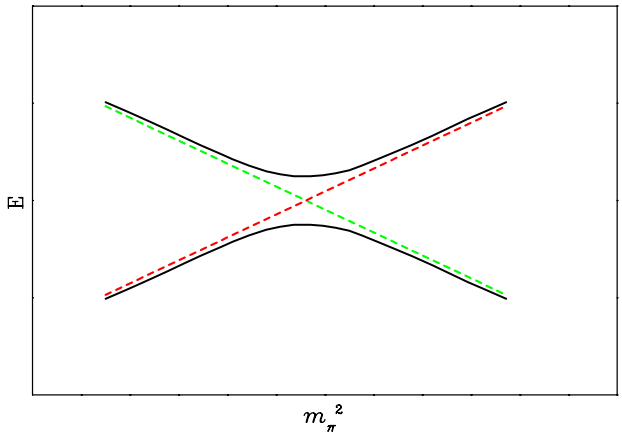

FIG. 3 (color online). Illustration of an avoided level crossing. The solid lines illustrate how the energy levels avoid crossing, while the two dotted lines illustrate how the nature of the associated eigenvectors flow. In the region where the energy states are closest each is an equal but orthogonal admixture of the two eigenvectors.

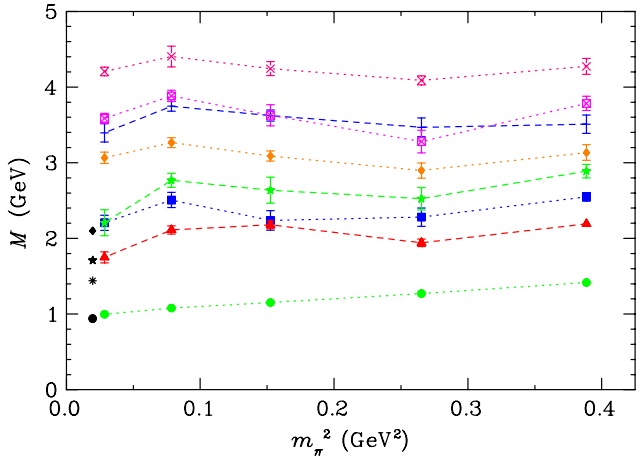

FIG. 4 (color online). As in Fig. 2, but with χ_1, χ_4 interpolators. The dotted lines in the figure connect similar eigenvectors.

the error bars. Results are presented as a function of quark mass (m_q), with $m_{q'} = \Delta m_q + m_q$ where Δm_q is small. In principle, as noted earlier a similar analysis can be performed for other lattice parameters in addition to the quark mass, such as the lattice spacing (a), volume (V), the lattice action etc.

The eigenvectors are also tracked for the correlation matrix analysis with the χ_1 and χ_4 interpolators and presented in Fig. 4, which can be compared with Fig. 2.

VI. QUARK-MASS FLOW OF EIGENSTATES

A. Positive parity

A key feature of large correlation matrices is the ability to identify and isolate energy eigenstates which are nearly degenerate in energy. However, this approximate degeneracy makes it difficult to trace the flow of states from one quark mass to the next. Thus a clear identification of these near-degenerate states through the features of the eigenvectors w^α isolating the states is necessary in order to trace the propagation of the states from the heavy to the light quark-mass region. At this point it is useful to clarify our use of language. Where we say eigenvector we are referring to the orthogonal eigenvectors, w^α, of our symmetric (or Hermitian) $M \times M$ correlation matrix $G(t)$. Where we speak of energy eigenvalues and energy eigenstates, we are referring to the eigenvalues and eigenstates of the lattice Hamiltonian, H. Our goal in calculations is always to choose the M interpolators well so that the few ($<M$) lowest eigenvalues extracted are a good approximation to the few lowest energy eigenvalues of H and so that M eigenvectors of our $M \times M$ correlation matrix $G(t)$ capture the dominant characteristics of the corresponding eigenstate of H.

The anticipated and relatively smooth flow of the eigenvectors as a function of the quark mass is presented in Fig. 5. It appears that each eigenvector corresponds to an energy eigenstate of H with the eigenvector w^α capturing some of the core properties of the corresponding full energy eigenstate of H. While the quark-mass dependent trends can be significant, our approach reliably allows the identification of energy eigenstates at adjacent quark masses.

As the χ_1 and χ_4 spin-flavor interpolators are very similar for the $N\frac{1}{2}^+$ channel, the overall flow of the eigenvectors $\vec{w}^\alpha$ obtained from the χ_1, χ_2 and χ_2, χ_4 correlation matrices are very similar in Fig. 5. Also, the overall strength of the eigenvector components creating and annihilating $N\frac{1}{2}^+$ energy states in the QCD vacuum remains approximately the same for the χ_1, χ_2 and χ_2, χ_4 cases (Fig. 6), which implies that the eigenstate-energies isolated by the χ_1, χ_2 and χ_2, χ_4 analysis are the same. As the first excited state is purely χ_1-spin-flavour dominated, this state is revealed in all the three different 8×8 correlation matrix analyzes.

There are a few general trends apparent in Figs. 6(a) and 6(b) which are worthy of note. Focusing on Fig. 6(a) for specific reference, we see that there is often competition between different smearing levels in creating the states. A good example is in state two, where the 200 sweep χ_1 interpolator is complemented by the 35 sweep χ_1 interpolator at heavy quark masses, but the 35 sweep interpolator strength is phased out as one approaches light quark masses with strength transitioning to the 100 sweep χ_1 interpolator. Even in the ground state one can see the importance of the 200 sweep interpolator increasing as one approaches the lighter masses. This effect is even stronger in Fig. 6(b) for the $\chi_4\chi_2$ analysis where the 100 sweep χ_4 operator is phased out in favour of the 200 sweep χ_4.

One can also observe the superposition of Gaussian smearings of different sizes being superimposed with

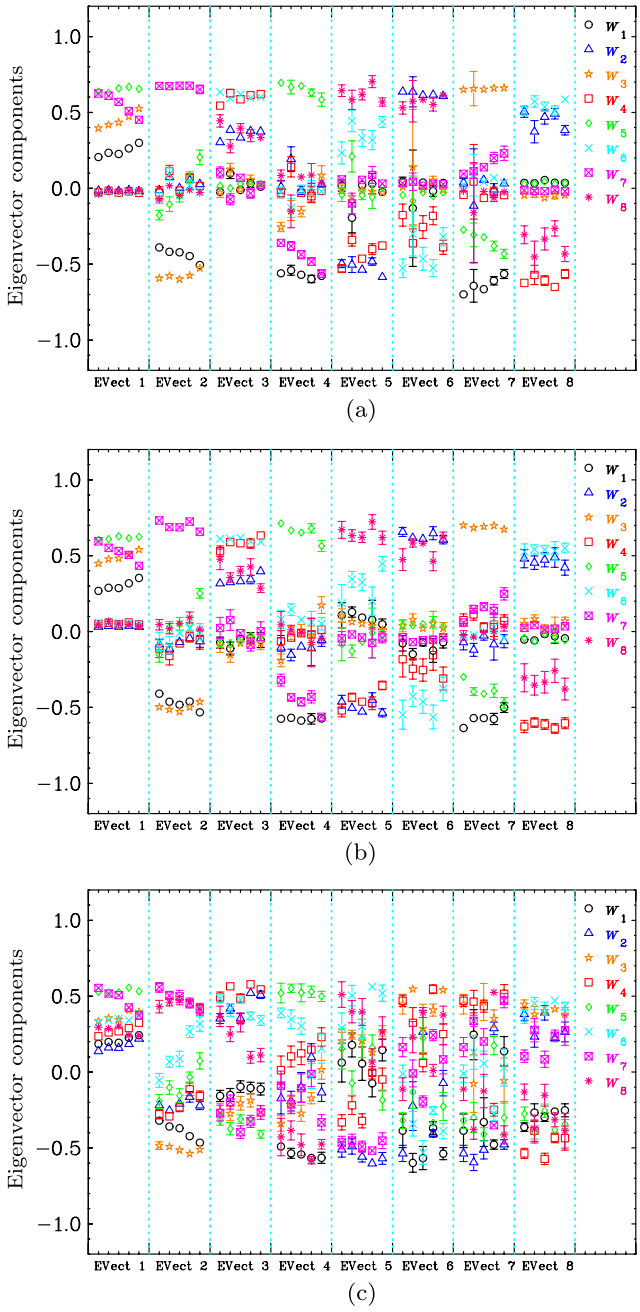

FIG. 5 (color online). $\vec{w}^{\alpha}$ is presented for the five different quark masses for the $N\frac{1}{2}^{+}$ channel after identifying eigenvectors via $\vec{w}^{\alpha}(m_q) \cdot \vec{w}^{\beta}(m_{q'})$. For each eigenvector shown in the horizontal axis, the eigenvector components are plotted in order of increasing quark mass from left to right. Note that Evect 1 to Evect 8 correspond to eigenvectors w^1 to w^8. In the legend, subscripts (1, 2), (3, 4), (5, 6) and (7, 8) correspond to the smearing-sweep levels of 16, 35, 100 and 200, respectively. (a) Eigenvector components for an 8×8 correlation matrix with χ_1, χ_2 interpolators. Odd and even numbers in the legend correspond to the χ_1 and χ_2, respectively. (b) As in Fig. 5(a), but for the χ_2 and χ_4 interpolators. Odd and even numbers in the legend correspond to the χ_4 and χ_2, respectively. (c) As in Fig. 5(a), but for the χ_1 and χ_4 interpolators. Odd and even numbers in the legend correspond to the χ_1 and χ_4, respectively.

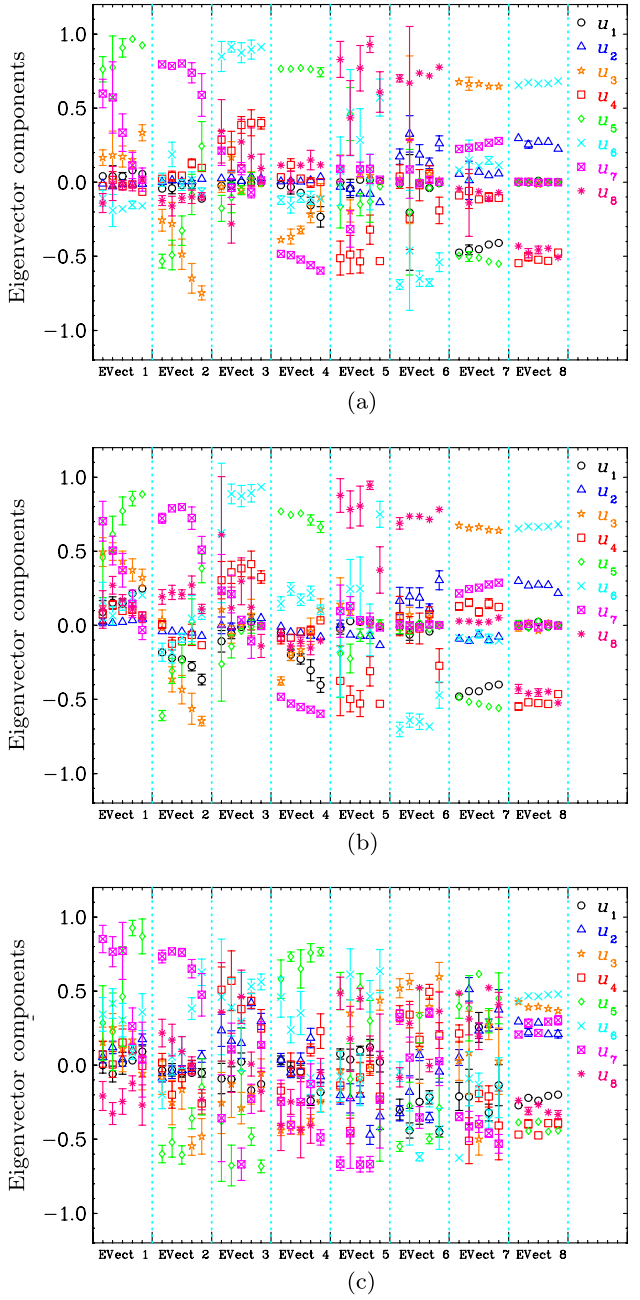

FIG. 6 (color online). $\vec{u}^{\alpha}$ is presented for the five different quark masses for the $N\frac{1}{2}^{+}$ channel. For each eigenvector shown in the horizontal axis, the eigenvector components are plotted in order of increasing quark mass from left to right. Note that Evect 1 to Evect 8 correspond to eigenvectors u^1 to u^8. In the legend, subscripts (1, 2), (3, 4), (5, 6) and (7, 8) correspond to the smearing-sweep levels of 16, 35, 100 and 200, respectively. (a) Eigenvector components for an 8×8 correlation matrix with χ_1, χ_2 interpolators. Odd and even numbers in the legend correspond to the χ_1 and χ_2, respectively. (b) As in Fig. 6(a), but for the χ_2 and χ_4 interpolators. Odd and even numbers in the legend correspond to the χ_4 and χ_2, respectively. (c) As in Fig. 6(a), but for the χ_1 and χ_4 interpolators. Odd and even numbers in the legend correspond to the χ_1 and χ_4, respectively.

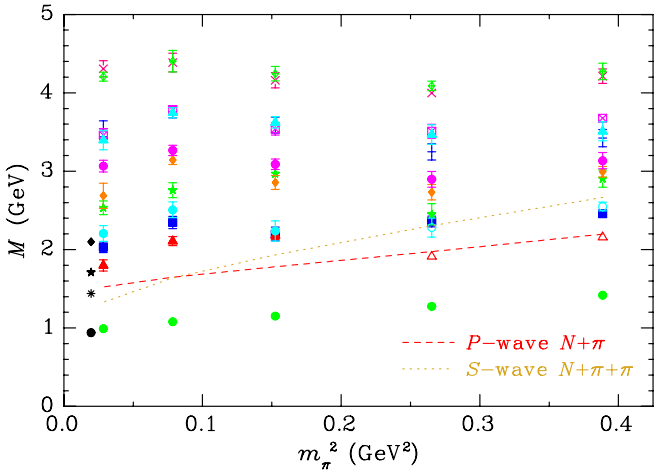

FIG. 7 (color online). $N\frac{1}{2}^+$ energy states from $8\times8\times2$ correlation matrices of χ_1, χ_2, χ_4 [29]. The p-wave $N\pi$ scattering threshold (with one unit of lattice momentum) and the s-wave $N\pi\pi$ threshold are presented by dashed and dotted lines, respectively.

relative minus signs in a manner that will create nodes in the radial wave function of the interpolator of Eq. (20). Focusing again on Fig. 6(a) to provide a specific example, consider state 2. Here the widest Gaussian of 200 sweeps is complemented by a smaller Gaussian with the opposite sign. Moreover, as the quark masses become light, the smaller Gaussian grows in size. The result is that the radial node position of the wave function increases in distance as the quarks become lighter.

Similarly, state 4 involves the superposition of three Gaussian smearings with alternating signs. Here the 200 sweep interpolator is complemented with the 100 sweep interpolator with opposite sign which is complemented further by the 35 sweep operator, again with the opposite sign. Such a linear combination can create two nodes in the radial wave function.

Finally, state 7 combines the 200, 100, 35 and 16 sweep interpolators with alternating signs such that a state with three nodes could be accessed.

Turning our attention to the $\chi_1\chi_4$ analysis, we see the flow of eigenvector components is not as smooth. Figures 5(c) and 6(c) present the flow of the eigenvectors for this analysis. A careful comparison of the eigenstate spectrum with that from the $\chi_1\chi_2$ analysis at each quark mass and consideration of the eigenvector flow of the states reveals that the states dominated by χ_1 in the $\chi_1\chi_2$ analysis are reproduced in the $\chi_1\chi_4$ analysis. However, the remaining four states display a flow different from those revealed in the $\chi_1\chi_2$ analysis. Thus, a superposition of the χ_1, χ_2 and χ_1, χ_4 analysis provides 12 unique energy states.

In Fig. 7, a superposition of the two 8×8 analysis ($8\times8\times2$) of χ_1, χ_2 and χ_1, χ_4 is presented. Scattering p-wave πN and s-wave $\pi\pi N$ energy levels are also shown.

For the two large quark masses, as seen in Fig. 7, the extracted lattice results sit close to the scattering two particle p-wave $N\pi$ threshold ($E_N + E_\pi$) with back-to-back momenta, $\vec{p} = (2\pi/L_x, 0, 0)$ and s-wave $N\pi\pi$ threshold ($M_N + M_\pi + M_\pi$), whereas the masses for the lighter three quarks sit much higher. There is no evidence of these scattering states at light quark masses. Our conclusion is that our 3-quark operators have very little coupling to the multihadron states relative to the states we do observe at the light quark masses.

It is noted that the couplings to the multiparticle meson-baryon states are suppressed by $1/\sqrt{V}$ relative to states

TABLE IV. The scalar product $\vec{w}^\alpha(m_q)\cdot\vec{w}^\beta(m_{q'})$, for $\kappa = 0.13700$ ($m_\pi = 702$ MeV) and $\kappa' = 0.13727$ ($m_\pi = 572$ MeV) (top left), $\kappa = 0.13727$ ($m_\pi = 572$ MeV) and $\kappa' = 0.13754$ ($m_\pi = 402$ MeV) (top right), $\kappa = 0.13754$ ($m_\pi = 402$ MeV) and $\kappa' = 0.13770$ ($m_\pi = 293$ MeV) (bottom left), $\kappa = 0.13770$ ($m_\pi = 293$ MeV) and $\kappa' = 0.13781$ ($m_\pi = 156$ MeV) (bottom right), for an 8×8 correlation matrix of χ_1 and χ_2, with four different levels of smearings, for the $N\frac{1}{2}^-$ states. States are ordered from left to right for $m_{q'}$ and top to bottom for m_q in order of increasing excited-state mass. α and β correspond to row and column, respectively.

−0.03	**0.99**	−0.08	−0.04	0.05	−0.01	0.00	0.01	−0.22	**0.97**	0.04	−0.10	−0.01	0.04	0.01	−0.02
1.00	0.02	0.01	−0.08	−0.02	−0.01	0.00	0.01	**0.97**	0.22	−0.07	−0.07	0.01	0.02	−0.02	−0.01
0.00	0.07	**0.97**	0.05	0.22	−0.03	−0.04	0.00	0.07	−0.03	**0.99**	−0.04	0.07	0.00	−0.02	−0.01
0.07	0.03	−0.07	**0.96**	0.01	−0.27	0.00	−0.02	0.05	0.11	0.04	**0.99**	−0.01	0.05	0.01	−0.04
−0.02	0.06	0.20	0.02	**−0.95**	−0.01	−0.23	−0.01	−0.01	0.02	−0.07	0.02	**0.99**	−0.09	0.04	0.03
0.03	0.02	0.01	0.26	0.00	**0.94**	−0.01	−0.21	0.02	0.04	0.01	0.04	−0.09	**−0.99**	−0.02	−0.02
−0.01	0.02	0.08	0.01	−0.22	0.01	**0.97**	0.01	0.02	−0.01	0.01	−0.01	−0.04	−0.01	**0.99**	−0.13
0.00	0.00	0.00	0.08	0.00	0.20	−0.02	**0.98**	0.01	0.02	0.02	0.03	−0.03	−0.02	0.12	**0.99**
0.91	0.40	0.02	0.02	0.01	−0.05	0.00	0.00	**0.98**	0.17	−0.06	−0.01	0.01	0.01	0.00	0.00
0.40	**−0.91**	0.00	0.01	−0.02	0.01	−0.01	0.00	−0.17	**0.99**	−0.01	−0.03	0.01	0.01	−0.01	0.00
−0.01	−0.01	**0.96**	−0.27	0.01	−0.01	0.00	0.02	0.05	0.03	**0.77**	0.64	−0.01	0.00	0.00	0.02
−0.03	0.00	0.27	**0.96**	0.01	0.01	0.02	0.00	0.04	−0.01	0.64	**−0.77**	−0.04	0.00	0.01	0.00
0.04	0.03	0.01	−0.01	−0.22	**0.97**	0.02	0.01	0.00	0.00	0.02	−0.01	0.66	**−0.75**	−0.04	−0.01
0.01	−0.01	−0.01	−0.01	**0.98**	0.22	0.04	0.00	−0.01	−0.01	0.03	−0.02	**0.75**	0.66	−0.04	−0.02
0.00	0.00	−0.02	0.01	0.01	−0.01	−0.12	**0.99**	0.00	0.01	0.00	0.01	0.05	−0.01	**0.96**	−0.26
0.01	−0.01	0.00	−0.02	−0.04	−0.03	**0.99**	0.12	0.00	0.00	−0.01	−0.01	0.04	0.01	0.26	**0.96**

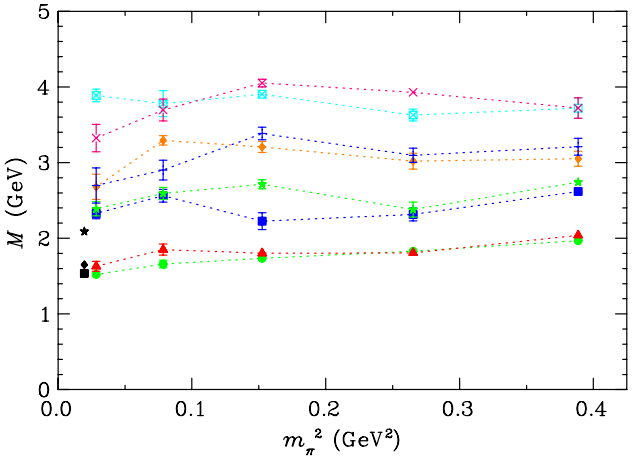

FIG. 8 (color online). Masses of $N\frac{1}{2}^-$ energy states from an 8×8 correlation matrix of χ_1, χ_2 in Table IV. The dotted lines in the figure illustrates the eigenvector flow.

dominated by a single-particle state. Due to the large volume of our lattice, it is likely that multiparticle states will be suppressed and missed in our spectrum, particularly at lighter quark masses where the quark-mass effect also acts to suppress the spectral strength. Further analysis of finite volume effects [51] on the spectrum is highly desirable. Future calculations should also investigate the use of five-quark operators to ensure better overlap with the multiparticle states and to better resolve and probe the excited state spectrum [35,42,43].

B. Negative parity

Now we can repeat our analysis for the identification of the $N\frac{1}{2}^-$ states. In Table IV, the scalar product $\mathcal{W}^{\alpha\beta} = \vec{w}^{\alpha}(m_q) \cdot \vec{w}^{\beta}(m_{q'})$ for all the quark masses is presented.

In Figs. 8 and 9, the $N\frac{1}{2}^-$ spectrum from the 8×8 analysis involving χ_1, χ_2 and χ_1, χ_4 is presented, respectively. While the χ_1, χ_4 analysis is able to extract a

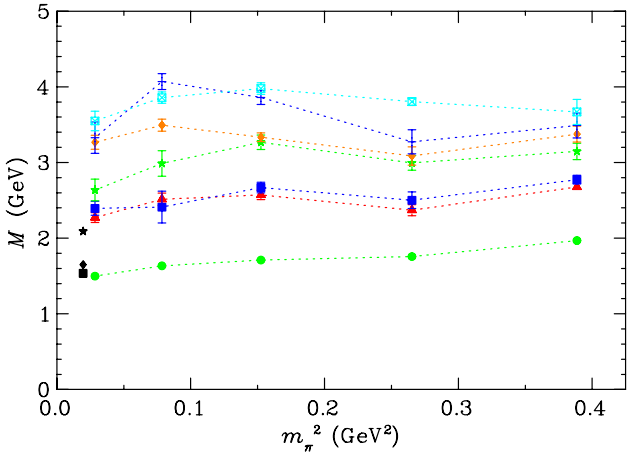

FIG. 9 (color online). As in Fig. 8, but with χ_1, χ_4 interpolators. The dotted lines in the figure illustrates the eigenvector flow.

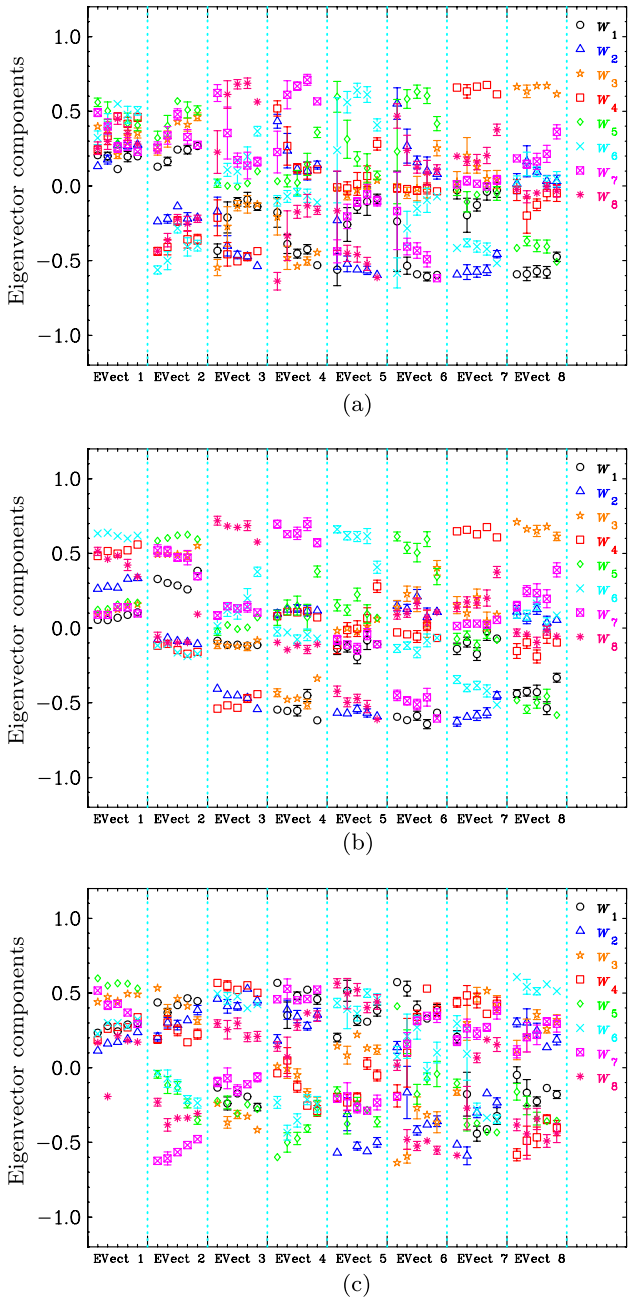

FIG. 10 (color online). $\vec{w}^{\alpha}$ for the five different quark masses are presented for the $N\frac{1}{2}^-$ channel after identifying eigenvectors via $\vec{w}^{\alpha}(m_q) \cdot \vec{w}^{\beta}(m_{q'})$. For each eigenvector shown in horizontal axis, the eigenvector components are plotted in order of increasing quark mass from left to right. Note that Evect 1 to Evect 8 correspond to eigenvectos w^1 to w^8. In the legend, subscripts (1, 2), (3, 4), (5, 6) and (7, 8) correspond to the smearing-sweep levels of 16, 35, 100, and 200, respectively. (a) Eigenvector components for an 8×8 correlation matrix with χ_1, χ_2 interpolators. Odd and even numbers in the legend correspond to the χ_1 and χ_2, respectively. (b) As in Fig. 10(a), but for χ_2 and χ_4 interpolators. Odd and even numbers in the legend correspond to the χ_4 and χ_2, respectively. (c) As in Fig. 10(a), but for χ_1 and χ_4 interpolators. Odd and even numbers in the legend correspond to the χ_1 and χ_4, respectively.

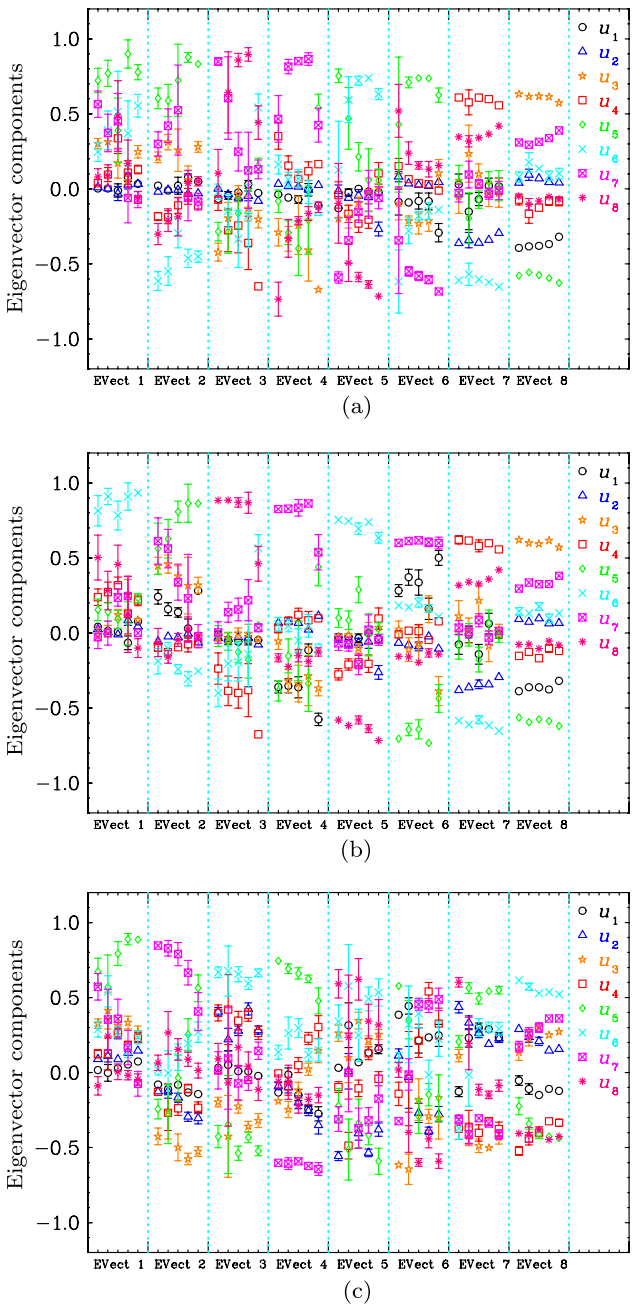

FIG. 11 (color online). $\vec{u}^{\alpha}$ for the five different quark masses are presented for the $N\frac{1}{2}^{-}$ channel. For each eigenvector shown in horizontal axis, the eigenvector components are plotted in order of increasing quark mass from left to right. Note that Evect 1 to Evect 8 correspond to eigenvectos u^1 to u^8. In the legend, subscripts (1, 2), (3, 4), (5, 6) and (7, 8) correspond to the smearing-sweep levels of 16, 35, 100 and 200, respectively. (a) Eigenvector components for an 8×8 correlation matrix with χ_1, χ_2 interpolators. Odd and even numbers in the legend correspond to the χ_1 and χ_2, respectively. (b) As in Fig. 11(a), but for χ_2 and χ_4 interpolators. Odd and even numbers in the legend correspond to the χ_4 and χ_2, respectively. (c) As in Fig. 11(a), but for χ_1 and χ_4 interpolators. Odd and even numbers in the legend correspond to the χ_1 and χ_4, respectively.

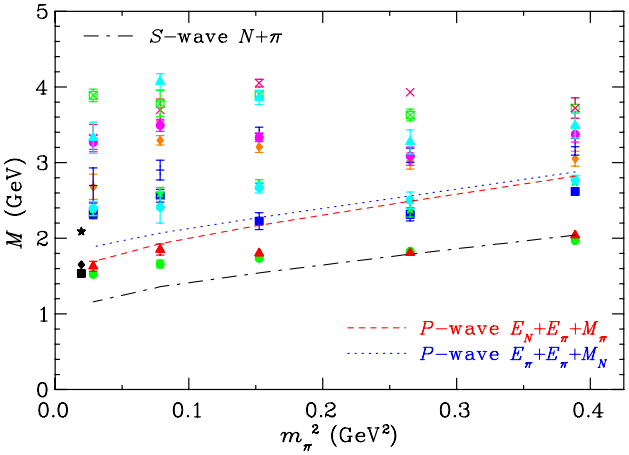

FIG. 12 (color online). Masses of $N\frac{1}{2}^{-}$ energy states from $8 \times 8 \times 2$ correlation matrices of χ_1, χ_2, χ_4.

low-lying energy state, it misses the near-degenerate second energy state in this channel. This second energy state is revealed in the χ_1, χ_2 spin-flavor combination presenting two nearly-degenerate low-lying states, which is in accord with the quark model based on $SU(6)$ spin-flavor symmetry. Recall that three spin-$\frac{1}{2}$ quarks may provide a total spin of $s = \frac{1}{2}$ or $\frac{3}{2}$, the $L = 1$ state can couple two different ways to provide a $J = \frac{1}{2}$ state, hence providing two orthogonal spin-$\frac{1}{2}$ states in the $L = 1, 70$ plet representation of $SU(6)$. Both of these states have a width of ≈ 150 MeV.

As in Fig. 5, the eigenvector components for different quark masses are presented in Figs. 10 and 11 for the $N\frac{1}{2}^{-}$ channel. It is interesting to note that the scalar-diquark interpolator χ_1 dominates the lowest two N^{-} states (Fig. 11) when available. The χ_2 interpolator makes an important contribution in creating the second energy state in this channel.

In Fig. 12, a superposition of the two 8×8 analysis ($8 \times 8 \times 2$) of χ_1, χ_2 and χ_1, χ_4 is presented. Scattering p-wave πN and s-wave $\pi\pi N$ states are also shown. The results for the lowest energy state at the two heavier pion masses sit close to the scattering s-wave $N + \pi$ ($M_\pi + M_N$) threshold indicating that these results may be scattering states at these pion masses. However, they disappear from our spectrum at the light pion masses. A similar situation also prevails the second energy state, where the state sits close to the p-wave $E_N + E_\pi + M_\pi$ and $E_\pi + E_\pi + M_N$ scattering threshold with back-to-back momenta of one lattice unit, $\vec{p} = (2\pi/L_x, 0, 0)$. Again the use of 5- or 7- etc. quark meson-baryon operators will be required to explore these scattering states [35,42,43].

VII. CONCLUSIONS

In this paper, a comprehensive analysis for the nucleon spectrum with $I = 1/2$, $s = 1/2$, is presented using the correlation matrix approach. In particular, a method for energy-eigenstate identification and flow is presented and

demonstrated for the positive and negative parity channel. Details of the method developed for an identification and the propagation of the energy states from heavy to light quark mass region are provided. In particular, the new technique is useful in identifying the flow of the near-degenerate energy eigenstates from one quark mass to the next. The eigenvectors obtained from the eigenvalue equations for several 8×8 correlation matrices are utilized in tracking the eigen-energy states.

In presenting the results, both nonsymmetric left and right eigenvalue equations and a symmetric eigenvalue equation are considered. While the masses are the same in the two different approaches, the eigenvectors obtained from the symmetric matrix are orthogonal. Thus the generalized measure $\mathcal{W}^{\alpha\beta}$ is used to track the flow of eigenvectors with quark mass. The scalar product of the eigenvectors shows its robustness in tracking the flow of the energy eigenstates even when the energies are nearly degenerate.

The coefficients of the interpolators creating and annihilating a state in the QCD vacuum are also presented. The flow of the eigenvectors reveals a smooth pattern and presents important insights into baryon structure and its evolution with quark mass.

Another interesting result of this paper is that, the correlation matrix method can be used to track the energy states that are involved in an avoided level crossing. It is noted that the avoided level crossings lie within the error bars, but the demonstration of the robustness of the approach remains.

Future steps include the introduction of five-quark meson-baryon operators in the correlation matrices, to ensure the clear isolation of states and ultimately extract the resonance parameters from the first principles of QCD.

ACKNOWLEDGMENTS

We thank PACS-CS Collaboration for making these $2 + 1$ flavor configurations available. This research was undertaken on the NCI National Facility in Canberra, Australia, which is supported by the Australian Commonwealth Government. We also acknowledge eResearch SA for generous grants of supercomputing time which have enabled this project. This research is supported by the Australian Research Council.

APPENDIX: PEDAGOGICAL DISCUSSION OF THE CORRELATION MATRIX

1. For $M = N$

Let us consider an N-dimensional Hilbert space with a Hamiltonian, $\hat{H}$, and let $|\chi_1\rangle, |\chi_2\rangle, \ldots, |\chi_N\rangle$ be N linearly independent states. Similarly, let $|E_1\rangle, |E_2\rangle, \ldots, |E_N\rangle$ be a complete orthonormal basis of energy eigenstates, then the state $|\chi_i\rangle$ can be written as

$$|\chi_i\rangle = \sum_{j=1}^{N} |E_j\rangle\langle E_j|\chi_i\rangle = \sum_{j=1}^{N} C_{ij}|E_j\rangle, \tag{A1}$$

where, $C_{ij} \equiv \langle E_j|\chi_i\rangle$, which is analogous to Eq. (7). In matrix form Eq. (A1) can be written as

$$\begin{bmatrix} |\chi_1\rangle \\ \vdots \\ |\chi_N\rangle \end{bmatrix} = [C] \begin{bmatrix} |E_1\rangle \\ \vdots \\ |E_N\rangle \end{bmatrix}. \tag{A2}$$

Since $|\chi_i\rangle$ is linearly independent, then C must be non-singular and so there must exist $(C^{-1})_{ij}$ such that

$$\begin{bmatrix} |E_1\rangle \\ \vdots \\ |E_N\rangle \end{bmatrix} = [C^{-1}] \begin{bmatrix} |\chi_1\rangle \\ \vdots \\ |\chi_N\rangle \end{bmatrix}. \tag{A3}$$

Similarly, $\langle\chi_i|$ can be expressed as $\langle\chi_i| = \sum_{j=1}^{N}\langle\chi_i|E_j\rangle \times \langle E_j| = \sum_{j=1}^{N} C^*_{ij}\langle E_j|$.

Let us now define $|\chi_i\rangle \equiv \hat{\chi}_i^\dagger|\Omega\rangle$ for N linearly independent field operators $(\hat{\chi}_i^\dagger)$, where the dagger denotes the adjoint. Then we may write

$$\begin{aligned} G_{ij}(t) &\equiv \langle\Omega|\hat{\chi}_i(t)\hat{\chi}_j^\dagger(0)|\Omega\rangle = \langle\Omega|\hat{\chi}_i e^{-i\hat{H}t}\hat{\chi}_j^\dagger|\Omega\rangle \\ &= \langle\chi_i|e^{-i\hat{H}t}|\chi_j\rangle = \sum_{k,l=1}^{N} C^*_{ik}\langle E_k|e^{-i\hat{H}t}|E_l\rangle C_{jl} \\ &= \sum_{k=1}^{N} C^*_{ik}e^{-E_k t}C_{jk} = \sum_{k=1}^{N} C^*_{ik}e^{-E_k t}(C^{*\dagger})_{kj} \end{aligned}$$

or,

$$\begin{aligned} [G(t)] &= [C^*]\begin{pmatrix} e^{-E_1 t} & 0 & 0 \\ 0 & e^{-E_2 t} & 0 \\ 0 & 0 & \ddots \end{pmatrix}[C^{*\dagger}] \\ &\equiv [C^*][E(t)][C^{*\dagger}], \end{aligned} \tag{A4}$$

where, $[E(t)]$ is obviously diagonal. The Eq. (A4) is analogous to Eq. (19). From this point on for notational convenience we will no longer use square brackets to denote matrices. We see that, $G(t) = G(t)^\dagger$ for all t. From Eq. (A4), we can also write

$$G(t_0) = C^*\sqrt{E(t_0)}\sqrt{E(t_0)}C^{*\dagger} = C'^*C'^{*\dagger}, \tag{A5}$$

where, $C'^* \equiv C^*\sqrt{E(t_0)}$ and $C'^{*\dagger} \equiv \sqrt{E(t_0)}C^{*\dagger}$. Similarly, we can write

$$G(t_0 + \triangle t) = C'^*E(\triangle t)C'^{*\dagger}. \tag{A6}$$

Let us consider the polar decomposition of C'^* as $C'^* = \sqrt{C'^*C'^{*\dagger}}U = \sqrt{G(t_0)}U$, where U is unitary

$$UU^\dagger = U^\dagger U = I.$$

Similarly, $C'^{*\dagger} = U^\dagger\sqrt{G(t_0)}$. Then, Eq. (A6) can be written as

$$G(t_0 + \triangle t) = \sqrt{G(t_0)}UE(\triangle t)U^\dagger\sqrt{G(t_0)} \tag{A7}$$

or equivalently

$$\begin{aligned}\tilde{G}(\triangle t) &\equiv \sqrt{G(t_0)}^{-1} G(t_0 + \triangle t)\sqrt{G(t_0)}^{-1} \\ &= UE(\triangle t)U^\dagger,\end{aligned} \tag{A8}$$

where we are using the notation

$$E(\Delta t) = \begin{bmatrix} e^{-E_1\Delta t} & 0 & 0 \\ 0 & e^{-E_2\Delta t} & 0 \\ 0 & 0 & \ddots \end{bmatrix}. \tag{A9}$$

Denoting the normalized eigenvectors of $\tilde{G}(\Delta t)$ as $\vec{w}^i$ for $i = 1, \ldots, N$, then U consists of columns $U = [\vec{w}^1|\vec{w}^2|\cdots|\vec{w}^N]$. Hence we see that

$$\tilde{G}(\Delta t)\vec{w}^i = e^{-E_i\Delta t}\vec{w}^i. \tag{A10}$$

Multiplying Eq. (A10) by $G(t_0)^{-1/2}$ from left and defining

$$\vec{u}^{\,i} \equiv G(t_0)^{-1/2}\vec{w}^i, \tag{A11}$$

gives

$$G(t_0)^{-1}G(t_0 + \Delta t)\vec{u}^i = e^{-E_i\Delta t}\vec{u}^i, \tag{A12}$$

which is analogous to Eq. (26).

2. For $M < N$

Let $\hat{\chi}_1, \hat{\chi}_2, \ldots, \hat{\chi}_N$ be M linearly independent interpolating field operators with $M < N$. Then we may consider these M $\hat{\chi}_i$'s as a subset of a complete set of N interpolating operators. Then as before, we can define $G^{(M)}(t)$ as an $M \times M$ correlation matrix, then $G^M(t)$ can be written as the upper left $M \times M$ block of $G(t)$ such that

$$G(t) = \begin{bmatrix} G^M(t) & G^m(t) \\ G^m(t)^\dagger & G^{(N-M)}(t) \end{bmatrix}, \tag{A13}$$

where the off-diagonal rectangular matrix $G^m(t)$ has elements $G^m_{ij}(t)$ for $i = 1, \ldots, M$ and $j = M + 1, \ldots, N$. Clearly $G^m(t)$ mixes the upper and lower diagonal blocks.

In terms of the full $N \times N$ correlation matrix $G(t)$ we define $\tilde{G}(\Delta t)$ as before and it has the form

$$\tilde{G}(\Delta t) = \begin{bmatrix} \tilde{G}^M(\Delta t) & \tilde{G}_m(\Delta t) \\ \tilde{G}_m(\Delta t)^\dagger & \tilde{G}^{(N-M)}(\Delta t) \end{bmatrix},$$

which is of course diagonalized by the full $N \times N$ unitary matrix U as shown in Eq. (A8).

Let us now temporarily assume that the off-diagonal elements of $\tilde{G}(\Delta t)$ are zero, then

$$\tilde{G}(\Delta t) = \begin{bmatrix} \tilde{G}^M(\Delta t) & 0 \\ 0 & \tilde{G}^{(N-M)}(\Delta t) \end{bmatrix},$$

and then it follows that the time independent unitary matrix can be written as

$$U = \begin{bmatrix} U^M & 0 \\ 0 & U^{(N-M)} \end{bmatrix}.$$

This will occur if and only if we have chosen our M interpolating fields such that they span exactly the same subspace as M of the exact energy eigenstates.

But we will certainly never exactly achieve this and so mixing will occur through $G^m(t) \neq 0$. In this case U will not have this convenient block diagonal form. Let U' diagonalize $\tilde{G}^M(\Delta t)$, i.e., U' is an $M \times M$ unitary matrix defined at this particular Δt. Then if $G^m(t) \neq 0$ we see that $U' \neq U^M$ and in general U' will not be independent of Δt. Note that M linearly independent interpolating field operators will operate on the vacuum and give rise to M linearly independent states. The more closely these M linearly independent states come to spanning the same subspace as M exact energy eigenstates, then the smaller will be $G^m(t)$ and the more block diagonal will be $\tilde{G}(\Delta t)$ and U. We can only ensure that $\tilde{G}^M(\Delta t)$ commutes with itself at all Δt if U is block diagonal, i.e., if $G^m(t) = 0$ so that $U' = U^M$ and is therefore time independent. Then the smaller will be the off-diagonal elements and the smaller will be the mixing and the excited state contamination.

In practice $M \ll N$, since on a lattice the dimensionality of Hilbert space is in the many millions. We would like to choose the M interpolating fields such that they span an M-dimensional subspace that has the greatest overlap possible with the subspace spanned by the M lowest energy eigenstates $|E_1\rangle, \ldots, |E_M\rangle$. With the lowest energy eigenstates our numerical errors will be minimized, since by working at large Euclidean times we minimize the influence of the higher excited state contamination and so optimize our extraction of the lowest M energy eigenstates.

Since the interpolating fields produced states $|\chi_i\rangle$ that were not normalized in any way, it is numerically convenient to redefine

$$\hat{\chi}_i(t) \to \hat{\chi}'_i(t) \equiv \frac{1}{\sqrt{G^M_{ii}(0)}}\hat{\chi}_i(t),$$

where there is no sum over i. Therefore, we attempt to put the strengths of our interpolating fields at a comparable level by defining

$$G'^M_{ij}(t) = \frac{1}{\sqrt{G^M_{ii}(0)}}G^M_{ij}(t)\frac{1}{\sqrt{G^M_{jj}(0)}}$$

to ensure that the matrix elements of $G'^M(t)$ are all $\sim\mathcal{O}(1)$ to maximize numerical significance of all "ij" combinations. This is completely legitimate as it is simply a change to the normalization chosen for our interpolating fields,

which we are free to do. The matrix $G'^M(t)$ is Hermitian except for the effects of finite ensemble and round-off errors. Let us define

$$\hat{G}^M(t) = \frac{1}{2}(G'^M(t) + G'^{M\dagger}(t)), \tag{A14}$$

as an improved unbiased estimator of the ensemble average for $G'^M(t)$. Then $\hat{G}^M(t)$ is exactly Hermitian. Therefore, as before, we may diagonalize

$$\tilde{\hat{G}}^M(\Delta t) \equiv [\hat{G}^M(t_0)^{-1/2}\hat{G}^M(t_0+\Delta t)\hat{G}^M(t_0)^{-1/2}], \tag{A15}$$

which is also Hermitian, as $\hat{G}^M(t_0)^{-1/2}$ and $\hat{G}^M(t_0+\Delta t)$ are obviously Hermitian. The eigenvectors $(\vec{w}^\alpha)$ obtained from diagonalizing the above matrix are therefore orthonormal. It is noted that using the $U + U^*$ trick [13], where these U's are links here, the Hermitian correlation matrix $G^M(t)$ is real symmetric and so the eigenvalues remain real and the eigenvectors orthogonal. Again, it is important to note that the more poorly we choose our M interpolating fields, the bigger will be the off-diagonal elements of $\tilde{\hat{G}}(t)$. Hence, the more time dependent will be the U' and the less reliable our extracted energies and eigenvectors.

Now we can consider $\hat{G}^M(t)$ as a function of quark mass, m_q, to identify how a given state evolves with m_q. If $m_q' = m_q + \Delta m_q$ with Δm_q small, we expect $\vec{w}^i(m_q).\vec{w}^j(m_q') \sim 1$ if $i = j$ and $\vec{w}^i(m_q).\vec{w}^j(m_q') \sim 0$ if $i \neq j$.

[1] S. Durr *et al.*, Science **322**, 1224 (2008).
[2] L. D. Roper, Phys. Rev. Lett. **12**, 340 (1964).
[3] N. Isgur and G. Karl, Phys. Lett. **72B**, 109 (1977).
[4] N. Isgur and G. Karl, Phys. Rev. D **19**, 2653 (1979).
[5] Z. Li, V. Burkert, and Z. Li, Phys. Rev. D **46**, 70 (1992).
[6] C. E. Carlson and N. C. Mukhopadhyay, Phys. Rev. Lett. **67**, 3745 (1991).
[7] P. A. M. Guichon, Phys. Lett. **164B**, 361 (1985).
[8] O. Krehl, C. Hanhart, S. Krewald, and J. Speth, Phys. Rev. C **62**, 025207 (2000).
[9] C. R. Allton *et al.* (UKQCD), Phys. Rev. D **47**, 5128 (1993).
[10] F. X. Lee and D. B. Leinweber, Nucl. Phys. B, Proc. Suppl. **73**, 258 (1999).
[11] M. Gockeler, R. Horsley, D. Pleiter, P. E. L. Rakow, G. Schierholz, C. M. Maynard, and D. G. Richards (QCDSF), Phys. Lett. B **532**, 63 (2002).
[12] S. Sasaki, T. Blum, and S. Ohta, Phys. Rev. D **65**, 074503 (2002).
[13] W. Melnitchouk, S. Bilson-Thompson, F. Bonnet, J. Hedditch, F. Lee, D. Leinweber, A. Williams, J. Zanotti, and J. Zhang, Phys. Rev. D **67**, 114506 (2003).
[14] R. G. Edwards, U. M. Heller, and D. G. Richards (LHP), Nucl. Phys. B, Proc. Suppl. **119**, 305 (2003).
[15] F. X. Lee, S. J. Dong, T. Draper, I. Horváth, K. F. Liu, N. Mathur, and J. B. Zhangd, Nucl. Phys. B, Proc. Suppl. **119**, 296 (2003).
[16] D. Brommel, P. Crompton, C. Gattringer, L. Glozman, C. Lang, S. Schaefer, and A. Schäfer (Bern-Graz-Regensburg), Phys. Rev. D **69**, 094513 (2004).
[17] N. Mathur, Y. Chen, S. J. Dong, T. Draper, I. Horváth, F. X. Lee, K. F. Liu, and J. B. Zhang, Phys. Lett. B **605**, 137 (2005).
[18] S. Sasaki, Prog. Theor. Phys. Suppl. **151**, 143 (2003).
[19] T. Burch, C. Gattringer, L. Glozman, R. Kleindl, C. Lang, and A. Schäfer (Bern-Graz-Regensburg), Phys. Rev. D **70**, 054502 (2004).
[20] S. Basak, R. Edwards, G. Fleming, K. Juge, A. Lichtl, C. Morningstar, D. Richards, I. Sato, and S. Wallace, Phys. Rev. D **76**, 074504 (2007).
[21] M. S. Mahbub, A. Ó Cais, W. Kamleh, B. Lasscock, D. Leinweber, and A. Williams, Phys. Rev. D **80**, 054507 (2009).
[22] M. S. Mahbub, A. Ó Cais, W. Kamleh, B. G. Lasscock, D. B. Leinweber, and A. G. Williams, Phys. Lett. B **679**, 418 (2009).
[23] G. T. Fleming, S. D. Cohen, H.-W. Lin, and V. Pereyra, Phys. Rev. D **80**, 074506 (2009).
[24] M. S. Mahbub, A. Ó Cais, W. Kamleh, D. B. Leinweber, and A. G. Williams, Phys. Rev. D **82**, 094504 (2010).
[25] M. S. Mahbub, W. Kamleh, D. B. Leinweber, A. Ó Cais, and A. G. Williams, Phys. Lett. B **693**, 351 (2010).
[26] J. M. Bulava *et al.*, Phys. Rev. D **79**, 034505 (2009).
[27] G. P. Engel, C. B. Lang, M. Limmer, D. Mohler, and A. Schafer (BGR [Bern-Graz-Regensburg]), Phys. Rev. D **82**, 034505 (2010).
[28] R. G. Edwards, J. J. Dudek, D. G. Richards, and S. J. Wallace, Phys. Rev. D **84**, 074508 (2011).
[29] M. S. Mahbub, W. Kamleh, D. B. Leinweber, P. J. Moran, and A. G. Williams (CSSM Lattice), Phys. Lett. B **707**, 389 (2012).
[30] H.-W. Lin and S. D. Cohen, AIP Conf. Proc. **1432**, 305 (2012).
[31] C. Michael, Nucl. Phys. **B259**, 58 (1985).
[32] M. Luscher and U. Wolff, Nucl. Phys. **B339**, 222 (1990).
[33] H.-W. Lin *et al.* (Hadron Spectrum), Phys. Rev. D **79**, 034502 (2009).
[34] J. Bulava, R. G. Edwards, E. Engelson, B. Joó, H.-W. Lin, C. Morningstar, D. G. Richards, and S. J. Wallace, Phys. Rev. D **82**, 014507 (2010).
[35] C. Morningstar, J. Bulava, J. Foley, K. J. Juge, D. Lenkner, M. Peardon, and C. H. Wong, Phys. Rev. D **83**, 114505 (2011).
[36] J. Bulava, Proc. Sci., LATTICE (2011) 021.
[37] B. J. Menadue, W. Kamleh, D. B. Leinweber, and M. S. Mahbub, Phys. Rev. Lett. **108**, 112001 (2012).
[38] R. G. Edwards, N. Mathur, D. G. Richards, and S. J. Wallace, Phys. Rev. D **87**, 054506 (2013).
[39] G. P. Engel, C. Lang, D. Mohler, and A. Schaefer, Phys. Rev. D **87**, 074504 (2013).

[40] S. Aoki *et al.* (PACS-CS), Phys. Rev. D **79**, 034503 (2009).
[41] M. S. Mahbub, W. Kamleh, D. B. Leinweber, P. J. Moran, and A. G. Williams (CSSM Lattice Collaboration), Phys. Rev. D **87**, 011501 (2013).
[42] C. Lang and V. Verduci, Phys. Rev. D **87**, 054502 (2013).
[43] C. Morningstar, J. Bulava, B. Fahy, J. Foley, Y. Jhang *et al.*, arXiv:1303.6816.
[44] S. Gusken, Nucl. Phys. B, Proc. Suppl. **17**, 361 (1990).
[45] B. Blossier, M. Della Morte, G. von Hippel, T. Mendes, and R. Sommer (ALPHA collaboration), J. High Energy Phys. 04 (2009) 094.
[46] M. G. Beckett, P. Coddington, B. Joó, C. M. Maynard, D. Pleiter, O. Tatebe, and T. Yoshie, Comput. Phys. Commun. **182**, 1208 (2011).
[47] Y. Iwasaki, arXiv:1111.7054.
[48] D. B. Leinweber, R. M. Woloshyn, and T. Draper, Phys. Rev. D **43**, 1659 (1991).
[49] D. B. Leinweber, Phys. Rev. D **51**, 6383 (1995).
[50] J. M. Zanotti, D. Leinweber, A. Williams, J. Zhang, W. Melnitchouk, and S. Choe (CSSM Lattice), Phys. Rev. D **68**, 054506 (2003).
[51] R. D. Young, D. B. Leinweber, A. W. Thomas, and S. V. Wright, Phys. Rev. D **66**, 094507 (2002).